Effect of electrostatic interaction on impact breakage of agglomerates formed by charged dielectric particles

Xuan Ruan and Shuiqing Li[*]

Key Laboratory for Thermal Science and Power Engineering of Ministry of Education, Department of Energy and Power Engineering, Tsinghua University, Beijing 100084, China

In this paper, the prototypical process of the normal impact of dense agglomerates is investigated using the discrete element method–boundary element method coupled simulations. The agglomerate consists of 50 charged particles with the surface energy equal to 10 mJ/m^2. The particles are assumed to be tribocharged and follow an exponential charge distribution, while the varying levels of coupled polarization are also considered. Simulation results reveal that the presence of the electrostatic interactions due to particle charging and polarization could drive more pronounced re-agglomeration after the collision, which effectively reduces the degree of agglomerate fragmentation. Moreover, when quantifying the collision outcomes using the fragmentation ratio, the influence of the electrostatic force is most significant at a moderate incident velocity. This is because, at such incident velocities, the impact is violent enough to break the agglomerate, but many ejected fragments are usually at low velocities and are attracted back by the long-range electrostatic force. Furthermore, the electrostatic force between same-sign particles even becomes attractive when particles are strongly polarized, leading to qualitative changes in particle dynamics. Finally, by comparing the collision outcomes under different incident velocities, the contact interactions are found to prevail when particles are still bounded in the agglomerate, while the electrostatic interaction becomes dominant after particles detach from each other.

I. INTRODUCTION

For micron-sized solid particles, the short-range van der Waals adhesion is strong compared with particle inertia, so microparticles could easily stick together and form agglomerates upon collisions [1–3]. The breakage of such agglomerates could significantly affect the size distribution, morphology, and even the reactivity of the solid phase, which is of great importance in various natural and industrial multiphase flows. Typical examples can be given as the formation of a planet [4,5], the removal of particulate matters [6,7], the transport of pharmaceutical powders [8,9], and the conveying of particle-laden flows [10,11]. Among different applications, the breakage of agglomerates can be roughly divided into two categories. The first is caused by hydrodynamic stress, where the agglomerates are stretched and even broken by surrounding fluid [12–17], while the latter is due to violent collisions of agglomerates with each other or with walls [18–21].

In this paper, the impact breakage of agglomerates on a solid wall is of particular interest for several reasons. First, the process of wall impact itself is almost inevitable in wall-bounded particulate flows [22], which affects the fragment size and particle movements. Additionally, the impact breakage can be employed as a prototypical process to investigate the dependence of agglomerate strength on various parameters [23,24]. Moreover, impact breakage has been applied as an efficient technology for solid particle dispersion [25,26]. To establish a clear link between the particle-scale interactions and the strength of the macroscopic agglomerates, detailed information, such as interparticle forces, is required. However, the characteristic time and length scales of impact breakage are extremely small, which makes it difficult to obtain desired information through experimental investigations. Hence, the discrete element method (DEM), which resolves the movements and contact interactions of individual particles, has been employed as a powerful tool to address this issue.

Extensive DEM simulations have been conducted to investigate the impact breakage under different parameters and configurations, which provide deep physical insights. For dry neutral particles, it is generally accepted that the short-range contact forces and torques could effectively resist interparticle movements and keep the agglomerates stable. Thornton *et al.* [23] performed two-dimensional simulations on the impact fragmentation of spherical agglomerates. The damage ratio of the interparticle contacts was found to scale with the dimensionless Weber number, which was defined as the ratio of the particle inertia to the surface adhesion. By assuming the energy required to break the contacts was proportional to the impact kinetic energy, Moreno-Atanasio and Ghadiri [24] included the effect of the elastic modulus. A modified dimensionless group was then proposed, which could describe well the breakage behavior within a wide range of surface energy. Apart from the normal impact of dense spherical agglomerates, the influences of different agglomerate structures, incident angles, and primary particle shapes have also been studied to extend the understanding further [20,27–30].

In addition to the intrinsic short-range contact interactions, particles could interact with each other through the long-range

*lishuiqing@tsinghua.edu.cn

electrostatic interaction. During handling and manufacturing, particles could easily get tribocharged through collisions [31–33]. The resulting long-range electrostatic force drastically alters particle behavior in various particle systems, such as particle packing [34], self-assembly [35], pore clogging [36,37], clustering in turbulence [38], and fluidization [39,40]. For the aggregation in granular flows, it has been reported that the presence of the electrostatic interaction remarkably increases the binding energy between charged grains and promotes the growth of large aggregates [41,42]. However, despite the ubiquity of triboelectrification and the significant role of the electrostatic interaction, the study on the impact breakage of charged agglomerates is still absent.

Additionally, when charged particles are very close to each other, the electrostatic force cannot be treated as the simple Coulomb force between point charges. Instead, charged particles become polarized, leading to more complicated electrostatic interactions that must be accurately accounted for. For instance, Kolehmainen *et al.* [43] adopted the induced dipole model to study particle-laden flows with various particle charging and polarization levels. It was found that particle polarization gave rise to distinct flow patterns that cannot be predicted by the point charge model. When considering the effect of the induced higher-order multipoles using the finite element method (FEM), the electrostatic force between a pair of polarized particles carrying same-sign charges could be attractive if the difference between the charges was significant [44]. This conclusion has recently been further extended to multiple particle situations for practical aggregation [45]. However, the accurate but expensive FEM has only been applied in static simulations, which limits further investigations on the dynamic process. As a result, efforts are still needed to unveil the influence of particle charging and polarization on the process of impact breakage.

To address the above issues, in this paper, we perform boundary element method (BEM)-DEM coupled simulations to investigate the impact breakage of dense spherical agglomerates formed by charged particles. Section II introduces the numerical methods used in this paper. The particle motions are evolved by the adhesive DEM, and the electrostatic interaction is accounted for using BEM. The generalized minimal residual (GMRES)–fast multipole method (FMM) algorithm is incorporated to achieve efficient electrostatic computation. Then simulation results are discussed in Sec. III. First, typical collision processes are displayed to compare the macroscopic collision outcomes between neutral and charged agglomerates. Scaling analysis is then conducted to illustrate the relative importance and respective dominant ranges of different interactions. Finally, by discussing the dominant factors under different incident velocities, the physical picture of impact breakage is presented.

II. METHODS

A. DEM

In this paper, the adhesive DEM is applied to evolve the translation and rotation of each particle [46,47]. The governing equations of particle motions are

given as

$$m\frac{d\mathbf{v}_i}{dt} = \sum_{j\neq i} \mathbf{F}_{ij}^{\mathrm{C}} + \mathbf{F}_i^{\mathrm{E}}, \tag{1a}$$

$$I\frac{d\mathbf{\Omega}_i}{dt} = \sum_{j\neq i} \mathbf{M}_{ij}^{\mathrm{C}} + \mathbf{M}_i^{\mathrm{E}}. \tag{1b}$$

Here, $m = 4\pi \rho_p r_p^3/3$ and $I = 2mr_p^2/5$ are the particle mass and the moment of inertia, where ρ_p and r_p are the particle density and radius. Also, $\mathbf{v}_i$ and $\mathbf{\Omega}_i$ are the velocity and the rotation rate of particle i. Furthermore, $\mathbf{F}_{ij}^{\mathrm{C}}$ and $\mathbf{M}_{ij}^{\mathrm{C}}$ are the contact force and torque exerted on particle i by another particle j. Then $\mathbf{F}_i^{\mathrm{E}}$ and $\mathbf{M}_i^{\mathrm{E}}$ are the electrostatic force and torque acting on particle i.

B. Contact interactions

If the center-to-center distance between two particles is smaller than the sum of their radius, these two particles are in contact, and the associated contact interactions are computed. In this paper, we consider various contact forces and torques due to four modes of relative motions, i.e., normal impact, sliding, rolling, and twisting.

The normal contact force is computed by the Johnson-Kendall-Roberts (JKR) theory together with the viscoelastic damping model (Appendix A). The JKR theory combines the effect of elastic repulsion and the van der Waals attraction [48], while the normal dissipation force is proportional to the normal relative velocity [49,50]. The resistance force/torques due to interparticle sliding, rolling, and twisting are modeled using the spring-dashpot-slider model. Here, spring terms depend on the relative displacements or rotation angles, and dashpot terms are proportional to the relative velocity or rotation rates. The slider model means, once exceeding the upper limits, the force/torques remain unchanged, and irreversible sliding, rolling, and twisting occur. Details of these models are given in Refs. [46,47,50] with their implementations introduced in our recent work [19,38].

C. BEM-based electrostatic calculation

In this paper, the BEM is employed to dynamically evolve the surface charge distribution on each particle surface. The electrostatic force and torque are then calculated through surface integration. This BEM-based method has been validated to accurately resolve the electrostatic interactions between charged spheres and ellipsoids. Here, only the key information of the BEM is introduced. For details, see Ruan *et al.* [51] and Barros *et al.* [52].

We start by looking at multiple charged dielectric particles in a vacuum [Fig. 1(a)]. The dielectric constant of the particles κ_p is uniform within each sphere, and the dielectric constant of the medium is κ_0. In this case, the dielectric constant κ only changes at the particle-medium interface, so the electrical charge only distributes on the particle surfaces, which is denoted by σ [52]. The surface charge density $\sigma(\mathbf{r})$ at a certain position $\mathbf{r}$ on the surface of particle i consists of both the free charge density σ_f and the induced charge density (or
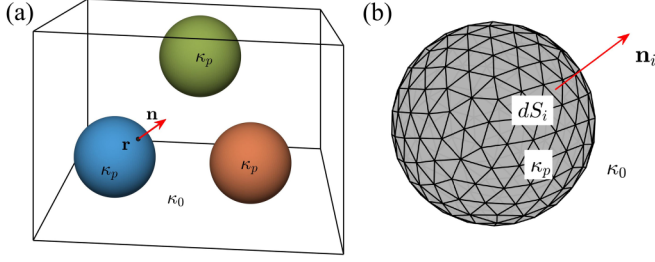
FIG. 1. Schematic of (a) the simulation system and (b) the triangular surface patches on a spherical particle.

the bound charge density) σ_b:

$$\sigma(\mathbf{r}) = \sigma_f(\mathbf{r}) + \sigma_b(\mathbf{r}). \tag{2}$$

Here, the free charge density σ_f is contributed by the uniform distribution of the net charge q_i carried by particle i, i.e., $\sigma_f = q_i/4\pi r_p^2$. In addition, since the dielectric particle can be polarized by the local electric field $\mathbf{E}(\mathbf{r})$ at $\mathbf{r}$, the bound charge density σ_b will be induced. To resolve the full surface charge distribution $\sigma(\mathbf{r})$, we need to solve for the unknown induced surface charge density $\sigma_b(\mathbf{r})$. The governing equation of σ_b has been derived in Ref. [51] as

$$\bar{\kappa}(\sigma_f + \sigma_b) + \varepsilon_0 \Delta\kappa \mathbf{E} \cdot \mathbf{n} = \sigma_f. \tag{3}$$

Here, $\bar{\kappa} = (\kappa_p + \kappa_0)/2$ and $\Delta\kappa = \kappa_0 - \kappa_p$ are the mean and difference of the dielectric constants of the particle and the medium, $\varepsilon_0 = 8.854 \times 10^{-12}$ F/m is the vacuum permittivity, and $\mathbf{n}$ is the unit vector along the outward normal direction at $\mathbf{r}$.

The full local field strength $\mathbf{E} = \mathbf{E}_f + \mathbf{E}_b + \mathbf{E}_{\text{ext}}$ contains three terms: (1) the field strength generated by all the free charge $\mathbf{E}_f$; (2) the field strength generated by all the induced charge $\mathbf{E}_b$, and (3) the external field $\mathbf{E}_{\text{ext}}$. To evaluate (1), the field strength $d\mathbf{E}_f$ at $\mathbf{r}_i$ generated by the free charge located at $\mathbf{r}_j$ can be determined using Green's function as

$$d\mathbf{E}_f(\mathbf{r}_i) = K(\mathbf{r}_i, \mathbf{r}_j)\sigma_b(\mathbf{r}_j)dS(\mathbf{r}_j)$$
$$= \frac{\mathbf{r}_i - \mathbf{r}_j}{4\pi\varepsilon_0|\mathbf{r}_i - \mathbf{r}_j|^3}\sigma_b(\mathbf{r}_j)dS(\mathbf{r}_j). \tag{4}$$

Here, $K(\mathbf{r}_i, \mathbf{r}_j) = (\mathbf{r}_i - \mathbf{r}_j)/4\pi\varepsilon_0|\mathbf{r}_i - \mathbf{r}_j|^3$ is the kernel function, and $\sigma_b(\mathbf{r}_j)dS(\mathbf{r}_j)$ is the total amount of charge located at $\mathbf{r}_j$. Then summing the contribution over all the surfaces S in the system yields

$$\mathbf{E}_f(\mathbf{r}_i) = \int_S K(\mathbf{r}_i, \mathbf{r}_j)\sigma_f(\mathbf{r}_j)dS(\mathbf{r}_j)$$
$$= \int_S \frac{\mathbf{r}_i - \mathbf{r}_j}{4\pi\varepsilon_0|\mathbf{r}_i - \mathbf{r}_j|^3}\sigma_f(\mathbf{r}_j)dS(\mathbf{r}_j). \tag{5}$$

Similarly, the second term $\mathbf{E}_b$ is the electric field generated by all the induced surface charge, which can be determined by substituting $\sigma_b(\mathbf{r}_j)$ for $\sigma_f(\mathbf{r}_j)$ in Eq. (5) as

$$\mathbf{E}_b(\mathbf{r}_i) = \int_S K(\mathbf{r}_i, \mathbf{r}_j)\sigma_b(\mathbf{r}_j)dS(\mathbf{r}_j)$$
$$= \int_S \frac{\mathbf{r}_i - \mathbf{r}_j}{4\pi\varepsilon_0|\mathbf{r}_i - \mathbf{r}_j|^3}\sigma_b(\mathbf{r}_j)dS(\mathbf{r}_j). \tag{6}$$

The third term $\mathbf{E}_{\text{ext}}$ is only nonzero if an external field exists. In this paper, the field strength is only generated by particle charge, so the external field is absent ($\mathbf{E}_{\text{ext}} = 0$). Therefore, we can rearrange Eq. (3) as

$$\bar{\kappa}\sigma_b + \varepsilon_0 \Delta\kappa \mathbf{E}_b \cdot \mathbf{n} = (1 - \bar{\kappa})\sigma_f - \varepsilon_0 \Delta\kappa \mathbf{E}_f \cdot \mathbf{n}. \tag{7}$$

According to Eq. (6), $\mathbf{E}_b$ relies linearly on σ_b, so the left-hand-side term of Eq. (7) can be further written as a linear form of σ_b:

$$A\sigma_b \equiv \bar{\kappa}\sigma_b + \varepsilon_0 \Delta\kappa \mathbf{E}_b \cdot \mathbf{n}, \tag{8}$$

while the right-hand-side term of Eq. (7) is also determined linearly by σ_f:

$$\mathbf{b} = (1 - \bar{\kappa})\sigma_f - \varepsilon_0 \Delta\kappa \mathbf{E}_f \cdot \mathbf{n}. \tag{9}$$

Thus, Eq. (7) can be written in a simpler form as

$$A\sigma_b = \mathbf{b}, \tag{10}$$

which separates the unknown σ_b from the known σ_f.

For each time step in the simulation, the physical parameters (κ_p and κ_0), the system geometry (particle location and size), and the free charge density σ_f are already known. We first solve Eq. (10) to obtain the induced charge density σ_b. It should be noted that, in the multiple-particle situation, Eq. (10) can be applied to the set of all the surface elements in the system regardless of which particle each surface element belongs to because all the surface elements interact with each other in the same way as described by Eq. (10). Then the full field strength $\mathbf{E} = \mathbf{E}_f + \mathbf{E}_b$ at each surface elements can be computed using Eqs. (5) and (6). The electrostatic force and torque acting on each particle can therefore be calculated by integrating the contribution over its surface S_i [51,52]:

$$\mathbf{F}_i^{\text{E}} = \int_{S_i} \kappa_0(\sigma_f + \sigma_b)\mathbf{E}(\mathbf{r})dS_i(\mathbf{r}), \tag{11a}$$

$$\mathbf{M}_i^{\text{E}} = \int_{S_i} \kappa_0(\sigma_f + \sigma_b)(\mathbf{r} - \mathbf{x}_i) \times \mathbf{E}(\mathbf{r})dS_i(\mathbf{r}). \tag{11b}$$

Here, $\mathbf{r} - \mathbf{x}_i$ is the vector pointing from the particle centroid $\mathbf{x}_i$ to each surface element $\mathbf{r}$.

It should be noted that the induced charge density σ_b does not change the net charge on each particle since the net charge q_i on each particle i is conserved:

$$\int_{S_i} (\sigma_f + \sigma_b)dS_i = q_i. \tag{12}$$

Instead, σ_b could effectively redistribute the surface charge due to particle polarization, which modifies the electrostatic interaction between particles. Also, the transfer of charge due to triboelectrification [53] is not considered in this paper.

D. Numerical implementation of BEM

1. Surface discretization

In the numerical simulation, the surface of each particle is discretized into triangular surface patches of similar size using the open-source code DISTMESH [54]. A typical example is shown in Fig. 1(b). In this paper, the number of surface patches on each particle is chosen as $N_{\text{pat}} = 392$, which is comparable with the settings in the previous study by Barros

and Luijten [55]. After the initial discretization, the location of each surface patch will be updated as particles translate and rotate in the domain, so there is no need to discretize particle surface every time step.

To resolve the surface charge distribution, we only need to solve the discretized form of Eq. (10), which is given in the index form as

$$A_{ij}\sigma_{b,j} = b_i. \tag{13}$$

Here, Einstein summation is applied to the repeated index j on the left-hand side. Also, $\sigma_{b,j}$ is the vector formed by the induced charge density of all the surface patches. The matrix A_{ij} contains the information of the geometry and the physical properties of the system

$$A_{ij} = \bar{\kappa}_i \delta_{ij} + \Delta \kappa_i \mathbf{n}_i \cdot \mathbf{I}_{ij} a_j. \tag{14}$$

Here, a_j is the area of the jth patch, δ_{ij} is the identity matrix, $\mathbf{I}_{ij}$ is the matrix consisting of the Green's function between each pair of surface patches:

$$\mathbf{I}_{ij} = \frac{\mathbf{r}_i - \mathbf{r}_j}{4\pi |\mathbf{r}_i - \mathbf{r}_j|^3}, \tag{15}$$

with $\mathbf{r}_i$ being the center location of the ith patch. The discretized form of the right-hand-side term in Eq. (9) is given in a similar way as

$$b_i = [(1 - \bar{\kappa}_i)\delta_{ij} - \Delta \kappa_i \mathbf{n}_i \cdot \mathbf{I}_{ij} a_j]\sigma_{f,j}. \tag{16}$$

Since the Green's function $\mathbf{I}_{ij}$ is singular for $i = j$, we neglect the electric field from one surface patch to its own center location ($\mathbf{I}_{ii} = \mathbf{0}$), which does not introduce significant deviations.

Taking Eqs. (14)–(16) into Eq. (13), we have

$$\bar{\kappa}_i \sigma_{b,i} + \Delta \kappa_i \mathbf{n}_i \cdot \mathbf{I}_{ij}\sigma_{b,j} a_j = (1 - \bar{\kappa}_i)\sigma_{f,i} - \Delta \kappa_i \mathbf{n}_i \cdot \mathbf{I}_{ij}\sigma_{f,j} a_j, \tag{17}$$

which is the discretized form of Eq. (7) considering the implicit summation over the repeated index j. Therefore, after the discretization, by solving Eq. (13) [or Eq. (17)], the induced charge density $\sigma_{b,j}$ at each patch j can be obtained.

When computing the electrostatic force and torque using Eq. (11), the field strength at the ith patch $\mathbf{E}(\mathbf{r}_i)$ is calculated by summing over the electric field generated by other ($N_{\text{tot}} - 1$) patches, where N_{tot} is the total number of surface patches in the system:

$$\mathbf{E}(\mathbf{r}_i) = \sum_{j \neq i} \frac{\mathbf{r}_i - \mathbf{r}_j}{4\pi \varepsilon_0 |\mathbf{r}_i - \mathbf{r}_j|^3} [\sigma_f(\mathbf{r}_j) + \sigma_b(\mathbf{r}_j)]a_j. \tag{18}$$

Therefore, direct calculation of the electric field at each patch leads to the computation cost of $O(N_{\text{tot}}^2)$, which is extremely expensive since N_{tot} is pretty large in the simulation. To reduce the calculation cost, the FMM is employed. When evaluating the electric field $\mathbf{E}(\mathbf{r}_i)$ at the target patch i, the electric field from close patches is directly accounted for using Eq. (18), while the electric field generated by far patches are approximated using the multipole expansion [56]. For an introduction on FMM, please see Appendix B and the references therein.

2. GMRES-FMM coupled algorithm

GMRES is applied to solve the linear equation Eq. (13) to find $\sigma_{b,j}$. For a brief introduction of GMRES, see Appendix C and the references therein. In the mth GMRES iteration, the mth-order Krylov subspace is generated using the matrix A_{ij} [Eq. (14)] and the vector b_i [Eq. (16)] as

$$K^{(m)} = \text{span}\{b_i, A_{ij}b_j, ..., A_{ij}^{m-1}b_j\}. \tag{19}$$

Please note that the index notation is used to represent the basis vectors in Eq. (19). Here, the free index $i = 1, 2, ..., N_{\text{tot}}$, with N_{tot} the total number of surface patches in the system. The dummy index j is summed over from 1 to N_{tot} since the Einstein summation is applied. For example, b_i is the vector defined by Eq. (16), $A_{ij}b_j$ refers to the matrix-vector product $A\mathbf{b}$, and $A_{ij}^{m-1}b_j$ denotes $A^{m-1}\mathbf{b}$.

Having constructed $K^{(m)}$, we determine the approximated solution $\sigma_{b,j}^{(m)}$ in $K^{(m)}$ by minimizing the norm of the residual $|r^{(m)}| = |b_i - A_{ij}\sigma_{b,j}^{(m)}|$ using the least square method. When the relative error is smaller than the preset limit $|r^{(m)}| \leqslant |b_i|/10^4$, the approximated value $\sigma_{b,j}^{(m)}$ is output as the final solution $\sigma_{b,j}$.

In the mth GMRES iteration, the most time-consuming step is to generate the new base vector $A_{ij}^{m-1}b_j$ through matrix-vector multiplication (i.e., $A^{m-1}\mathbf{b} = A \times A^{m-2}\mathbf{b}$). The calculation cost scales as $O(N_{\text{tot}}^2)$. To accelerate the calculation, the matrix-vector multiplication can be treated as a forward electrostatic problem, which is explained as follows. In the previous iteration, $A^{m-2}\mathbf{b}$ is already known. By defining the fake charge density vector $\sigma_{fk} = A^{m-2}\mathbf{b}$, the product becomes

$$A^{m-1}\mathbf{b} = A \times A^{m-2}\mathbf{b} = A\sigma_{fk}. \tag{20}$$

Taking in Eqs. (14) and (15), Eq. (20) can be written in the index notation as

$$A_{ij}^{m-1}b_j = A_{ij}\sigma_{fk,j} = \bar{\kappa}_i\sigma_{fk,i} + \Delta\kappa_i\mathbf{n}_i \cdot \frac{\mathbf{r}_i - \mathbf{r}_j}{4\pi|\mathbf{r}_i - \mathbf{r}_j|^3}\sigma_{fk,j}a_j. \tag{21}$$

Considering the summation over the dummy index j, the second term on the right-hand side of Eq. (21) is to evaluate the electric field generated by other patches at the position of the ith patch. The problem of calculating the matrix-vector product is hence converted to the problem of solving the electric field generated by the fake charge density vector σ_{fk}. Therefore, the FMM can by implemented to accelerate the computation. In this paper, the open-source library FMMLIB3D [57] is incorporated in GMRES iteration to achieve the efficient electrostatic calculation [58].

3. Double-shell model

As introduced in Sec. II B (and Appendix A), a positive overlap δ_N is required to calculate the contact interactions between two particles. However, if two surface patches intersect with each other, the electric field evaluated by Eq. (18) will diverge. We therefore propose the double-shell model to address this issue.

As shown in Fig. 2(a), the patches used in the electrostatic calculation locate on the original particle surface (gray
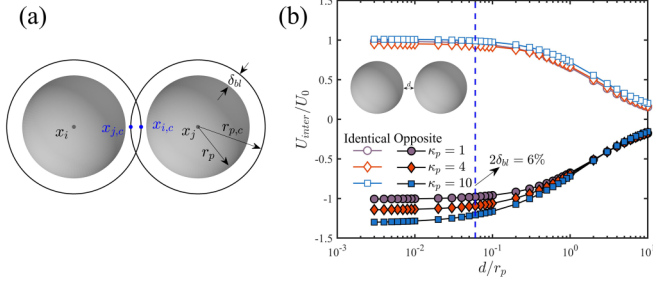
FIG. 2. (a) Schematic of the two-shell model. (b) The normalized electrostatic interaction energy U_{inter}/U_0 between two charged dielectric particles with varying levels of polarization.

FIG. 3. Agglomerate structure.

surfaces), while a slightly larger collision shell (black profiles) is used to compute the contact interactions. Here, $\mathbf{x}_{i,c}$ and $\mathbf{x}_{j,c}$ in Fig. 2(a) are the contact points on particle i and j, respectively. The collision radius equals $r_{p,c} = r_p + \delta_{\text{bl}}$, with δ_{bl} being the thickness of the buffer layer between two parallel shells.

The value of δ_{bl} is chosen for two reasons: (i) the buffer layer should be thin enough to minimize the error due to the noncoincidence of two shells and (ii) the buffer layer should always be thicker than the maximum normal overlap in collisions to avoid the intersection of surface patches. For (i), we calculate the electrostatic interaction energy (see Appendix D) between two identically or oppositely charged dielectric particles with different separation distances.

Figure 2(b) plots the normalized interaction energy U_{inter}/U_0 as a function of the normalized gap d/r_p. Here, $U_0 = 2\pi r_p^3 \sigma_f^2/\varepsilon_0$ is the characteristic electrostatic energy, where σ_f is the magnitude of the free charge density. For identically charged particles, U_{inter}/U_0 continues to rise as d/R decreases because two particles must overcome the electrostatic repulsion to get closer. If the polarity is opposite, the decreasing trend is observed as expected. Despite the charge polarity and different dielectric constants κ_p, U_{inter}/U_0 almost saturates when $d/r_p \leqslant 0.1$, which indicates that the electrostatic energy will not change significantly if two particles are sufficiently close. If we set the buffer layer thickness as $\delta_{\text{bl}}/r_p = 3\%$, the separation distance between two colliding particles is no larger than $2\delta_{\text{bl}} = 6\% r_p$ [dashed line in Fig. 2(b)], which meets the requirement of (i). Additionally, the maximum normal overlap in this paper satisfies $\delta_{\text{max}}/r_p \leqslant 0.5\%$, so the surface patches do not intersect in the dynamic simulations.

E. Agglomerate formation

The dense spherical agglomerates are generated using the method of centripetal packing [14,59]. Fifty primary particles are first randomly placed in the spherical space with no overlap and zero velocity. The artificial centripetal force, whose magnitude is 10 times that of gravity, is acted on each particle. When being driven toward the domain center, the primary particles encounter collisions and agglomerate. Eventually, one giant agglomerate containing all the primary particles is formed. The centripetal force is then removed to relieve the internal stresses in the agglomerate. After reaching the equilibrium state, the agglomerate structures are directly
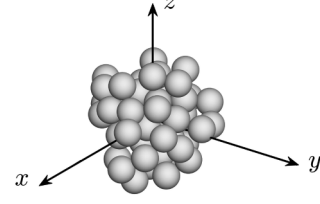
extracted and used in the wall impact simulations. In the packing process, the electrostatic force is not included, so the agglomerate structure is determined by the competition between the driving force (centripetal force) and the resistant forces (contact forces/torques).

Figure 3 displays a typical agglomerate structure obtained from the centripetal packing. The gyration radius R_g is adopted to measure the agglomerate size and given as

$$R_g = \left[\frac{1}{N_p} \sum_{i=1}^{N_p} (\mathbf{x}_i - \mathbf{x}_c)^2 \right]^{1/2}, \tag{22}$$

where $\mathbf{x}_c = \sum_{i=1}^{N_p} \mathbf{x}_i/N_p$ is the position of the mass center of the agglomerate, N_p is the number of primary particles in the agglomerate. Here, the ratio between the gyration radius R_g and the particle collision radius $r_{p,c}$ equals $R_g/r_{p,c} = 3.64$, and there are 59 interparticle contacts. The fractal dimension of the agglomerate is $D_f = 2.82 \pm 0.03$, indicating that the structure is close to a dense spherical one ($D_f \approx 3$) [14].

In this paper, we simulate the breakage of agglomerates containing $N_p = 50$ primary particles. This particle number leads to the computation cost of resolving $N_{\text{tot}} = 19\,600$ surface patches in the electrostatic calculation, which is within the reasonable range. Meanwhile, a recent study has shown that a 50-particle agglomerate is already enough to reveal the essential physics in the impact breakage process [20].

F. Simulation conditions

In each simulation, the agglomerate is initially placed over an infinite wall, and the normal impact velocity v_{im} is assigned to each primary particle. When the simulation starts, both the electrostatic force and the contact interactions are simultaneously added, so the agglomerate starts to restructure as it moves downward. The distance between the initial position of the agglomerate and the wall is long enough so that the agglomerate has become stable again before the impact. In fact, since the initial structure is compact ($D_f = 2.82 \pm 0.03$), all the primary particles are bound by the contact interactions, so the structures remain almost the same for different neutral/charging conditions before each impact. The simulation continues until the impact process is finished and no more significant changes can be observed. By varying the incident velocity v_{im} and the dielectric constant of the particle κ_p, the effect of the electrostatic interaction on the impact breakage is studied.

Since the collision outcome can be affected by the impact point on the agglomerate surface and the particle charge distribution, we perform parallel runs for the same v_{im} and κ_p. In each run, the agglomerate is first rotated about the x or y
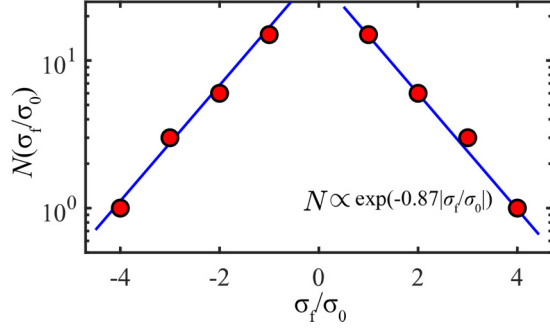
FIG. 4. Exponential distribution of the number of particles carrying the normalized free charge density σ_f/σ_0.

axis before the simulation starts, and the associated impact point on the agglomerate surface is changed. Here, the initial rotation angles along the x and y axes are (1) $\theta_x = 0$, $\theta_y = 0$, (2) $\theta_x = \pi/2$, $\theta_y = 0$, and (3) $\theta_x = 0$, $\theta_y = \pi/2$. Extra simulations have been run with more initial rotation angles, and the results show no noticeable difference. Therefore, the results of three groups of initial rotation angles are already representative enough.

As for the distribution of the free charge, we assume that the net charge carried by the particles is not identical and follows the exponential distribution (Fig. 4):

$$N \propto \exp\left(-0.87\left|\frac{\sigma_f}{\sigma_0}\right|\right). \tag{23}$$

Here, $N(\sigma_f/\sigma_0)$ is the number of particles carrying the free charge density σ_f, and σ_0 is the characteristic charging density. This assumption is consistent with previous experimental observations on tribocharged particles [42]. Therefore, half of the particles are positively charged, and the other half are negatively charged. For the magnitude of free surface charge, most particles carry a small amount of charge, while several particles are highly charged. To make sure that the simulation results do not rely on a specific charge distribution, for the same rotation angles (θ_x, θ_y), three parallel runs are performed using different realizations of the free charge distribution.

When computing the contact forces and torques, the wall is treated as a particle with an infinite radius. Nevertheless, the wall is noninteractive in electrostatic calculation because the wall effect in electrostatic calculation can be regarded as a separate problem and is beyond the scope of this paper [60,61].

Table I lists the simulation parameters. The particle density, the elastic modulus, and Poisson's ratio are related to SiO$_2$ particles [20,50]. The surface energy density of the solid particle is defined as [1]

$$\gamma = \frac{A_H}{24\pi\delta_{\min}^2}, \tag{24}$$

where A_H is the Hamaker constant of the given material. For common materials, the value of A_H lies within the range 10^{-21} to 10^{-19} J in the vacuum. Here, $\delta_{\min}$ is the minimum separation distance between two contacting surfaces. Based on experimental measurements, the recommended value of $\delta_{\min}$ is $0.15 - 0.40$ nm. Here, we choose $\delta_{\min} = 0.165$ nm, as

TABLE I. Simulation parameters.

Physical parameters	Values	Units
Particle radius (r_p)	10	μm
Buffer layer thickness (δ_{bl})	0.3	μm
Particle density (ρ_p)	2500	kg/m^3
Elastic modulus (E)	10^{10}	Pa
Poisson's ratio (σ_p)	0.33	—
Restitution coefficient (e)	0.7	—
Friction factor (μ_F)	0.3	—
Surface energy density (γ)	10	mJ/m^2
Characteristic charging density (σ_0)	5	μC/m^2
Dielectric constant of particle (κ_p)	1, 4, 10	—
Dielectric constant of medium (κ_0)	1	—
Incident velocity (v_{im})	0.08–0.5	m/s

suggested by Marshall and Li [50], which gives the range of γ as $O(10^{-1})$–$O(10^1)$ mJ/m^2. The value of the surface energy density ($\gamma = 10$ mJ/m^2) is thus within the common range of SiO$_2$ particles, which characterizes the strength of the van der Waals adhesion (Appendix A). The characteristic charging density is $\sigma_0 = 5\,\mu$C/m^2, which is comparable with the experimental measurements due to triboelectrification [62,63]. Three typical values of the particle dielectric constant are used here (i.e., $\kappa_p = 1, 4, 10$). Here, $\kappa_p = 1$ refers to the ideal condition that particles cannot be polarized, while the last two values are close to that of a SiO$_2$ particle ($\kappa_p = 4$) and a SiO$_2 - ZrO_2$ fused particle ($\kappa_p = 10$) [41]. The friction factor μ_F is chosen based on experimental measurements [64].

One vital issue in the simulation is the choice of the simulation time step dt_C. The time step should be much smaller than the characteristic collision time scale τ_C to describe the rapid variating collision interactions. The characteristic collision time scale can be estimated by $\tau_C \sim (\rho_p^2/E^2 v_C)^{1/5} r_p$ where v_C is the collision velocity [50]. In this paper, the smallest collision time scale is of the order of 10^{-7} s, and the collision time step is chosen as $dt_C = 2.5 \times 10^{-9}$ s so that $dt_C/\tau_C < 2\%$. Additionally, it is not necessary to compute the electrostatic interaction at each collision time step because particles do not move significantly within dt_C, and the electrostatic interaction is almost the same. Instead, the electrostatic interaction is updated at a large time step $dt_E = 40dt_C = 10^{-7}$ s. Particles only travel a small distance compared with their radius within dt_E (i.e., $v \cdot dt_E \leqslant 1\%r_p$), so the variation of the electrostatic interaction is captured accurately as particles move.

III. RESULTS AND DISCUSSIONS

A. Effect of the electrostatic force on the collision process

We start by investigating the impacts of the electrostatic interaction on typical collision outcomes. Figure 5 displays snapshots of the impact breakage of neutral and charged agglomerates with the same impact point and incident velocity $v_{im} = 0.25$ m/s. After colliding with the wall, the agglomerate first undergoes significant compression and deformation, followed by further fragmentation.

For neutral particles shown in Figs. 5(a), 5(d), and 5(g), the free charge density σ_f is zero, so there is no electro-
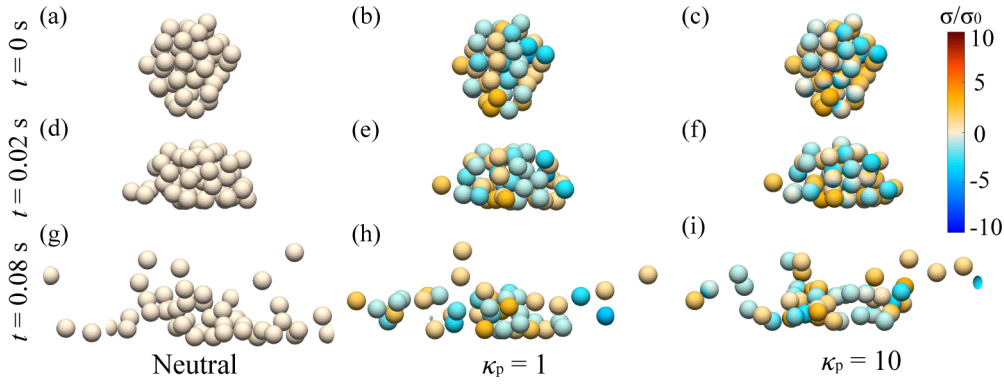
FIG. 5. (a), (d), and (g) Impact breakage of neutral particles, (b), (e), and (h) charged particles with $\kappa_p = 1$, and (c), (f), and (i) $\kappa_p = 10$ at three instants. The incident velocity is $v_{\text{im}} = 0.25$ m/s. The color bar denotes the normalized surface charge density σ/σ_0.

static interaction between particles. For charged particles, the exponential distribution of σ_f is assigned randomly to different particles. If $\kappa_p = 1$, the induced surface charge density σ_b remains zero, so the surface charge is only contributed by the free charge density σ_f, which distributes uniformly on the surface of each particle [Figs. 5(b), 5(e), and 5(h)]. For $\kappa_p = 10$, particles are significantly polarized under the electric field, leading to the highly nonuniform charge distribution on individual particle surfaces shown in Figs. 5(c), 5(f), and 5(i). Therefore, BEM proves to capture the dynamic evolution of the surface charge distribution well during the impact process.

We now show that, in addition to the different surface charge distributions, the charged agglomerates show a weaker tendency to break at $t = 0.08$ s [Figs. 5(g), 5(h), and 5(i)]. To better describe the differences in Fig. 5, we analyze the interparticle contact network at each time step and plot the temporal evolution of the number of agglomerates N_{agg} in Fig. 6. Before the collision, all the particles are contained in the initial agglomerate, so $N_{\text{agg}} = 1$ at $t = 0$ s. After the collision occurs, the agglomerate is quickly compressed, accompanied by the rapid breakup of interparticle contacts. As a result, the initial agglomerate breaks into many small frag-

ments, leading to the sudden rise of N_{agg}. The fragments then start to rebound and collide with each other. Some fragments may stick together and re-agglomerate, causing the decrease of N_{agg} after the peak around $t = 0.02$ s. As the fragments continue to separate, no more pronounced changes are observed, so N_{agg} eventually reaches a steady state.

When comparing different charging conditions, the N_{agg} curves coincide at the initial compression stage ($t = 0 - 0.012$ s). During this stage, the collision is energetic enough to break the contacts rapidly regardless of the electrostatic interactions. Then N_{agg} curves for the charged cases are found to reach their peaks earlier compared with the neutral case ($t = 0.012 - 0.02$ s), and the peak values also become lower, indicating less fragmentation of the agglomerate after the initial compression stage. In the later rebound and re-agglomeration stage ($t = 0.02 - 0.08$ s), charged particles are more likely to get attracted back and re-agglomerate, giving rise to a faster decrease of N_{agg}. When considering the induced surface charge σ_b for $\kappa_p = 10$, the re-agglomeration becomes more significant, indicating that particle polarization may further enhance the stability of the agglomerate.

To evaluate the fragmentation in a quantitative manner, we define the fragmentation ratio Θ_{fr} as [20]

$$\Theta_{\text{fr}} = \frac{N_{\text{agg}} - 1}{N_{\text{agg,max}} - 1}. \tag{25}$$

Here, N_{agg} is the number of agglomerates at the final steady state (Fig. 6), and $N_{\text{agg,max}}$ is the maximum number of agglomerates that can be produced, i.e., the number of primary particles N_{par}. If the initial agglomerate does not break, the fragmentation ratio $\Theta_{fr} = 0$. In contrast, if the agglomerate breaks into 50 single particles, the ratio becomes $\Theta_{fr} = 1$.

As introduced in Sec. II F, by performing parallel simulations with three different impact points and three realizations of the charge distribution, we take statistics of Θ_{fr} to illustrate the effects of the electrostatic interaction on the collision outcomes. As a result, three (nine) parallel simulations are performed for each neutral (charged) case.

Figure 7(a) shows the fragmentation ratio Θ_{fr} as a function of the incident velocity v_{im}. The scatters denote the average value, and the bars refer to the standard deviations. For neutral particles, the agglomerate experiences more complete fragmentation in a more violent collision, so Θ_{fr} increases from 0 to 1 as v_{im} increases. For the same v_{im}, if particles are charged,
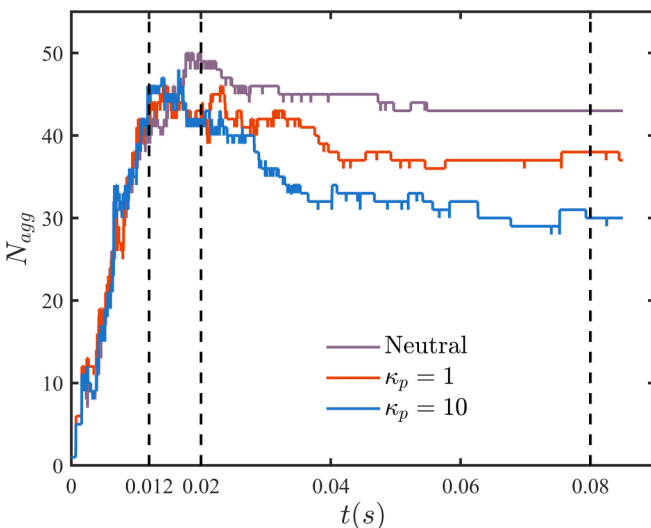

FIG. 6. Temporal evolution of the number of agglomerates N_{agg} in the collision processes shown in Fig. 5.
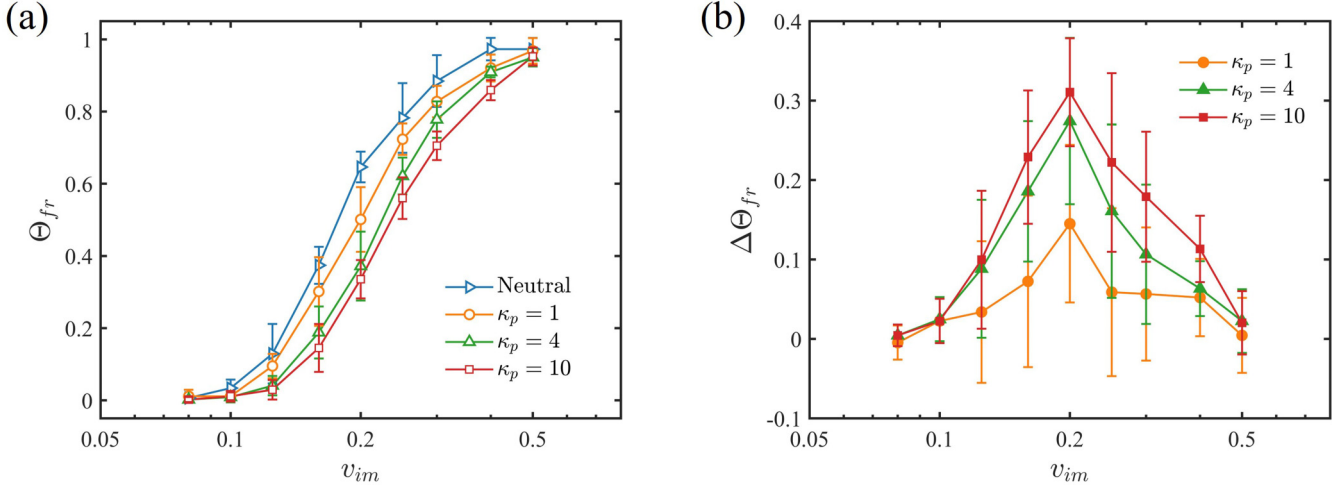
FIG. 7. (a) Fragmentation ratio Θ_{fr} as a function of the incident velocity v_{im}. (b) Change of Θ_{fr} compared with neutral particles.

Θ_{fr} will decrease because of the re-agglomeration shown in Fig. 6. The decreasing trend becomes more pronounced as κ_p increases, revealing a nonnegligible effect of particle polarization. Therefore, we emphasize the need to consider the induced surface charge in applications where particles are sufficiently close.

We then calculate the change of Θ_{fr} as

$$\Delta\Theta_{\text{fr}} = \Theta_{\text{fr,Neu}} - \Theta_{\text{fr,Ch}}, \qquad (26)$$

to measure the decreased extent of fragmentation because of the electrostatic interaction. Here, $\Theta_{\text{fr,Neu}}$ and $\Theta_{\text{fr,Ch}}$ are the fragmentation ratio of neutral and charged agglomerates, respectively. The dependence of $\Delta\Theta_{fr}$ on v_{im} is plotted in Fig. 7(b). Here, $\Delta\Theta_{fr}$ first increases with v_{im} and peaks around $v_{\text{im}} = 0.2$ m/s. As v_{im} further increases, however, $\Delta\Theta_{fr}$ starts to go down and approaches zero, indicating that the influence of the electrostatic force is only profound within a moderate v_{im} range.

B. Scaling analysis of electrostatic and contact interactions

In the simulation, particle movements are affected by both the electrostatic and contact interactions. In this section, we study the relative importance of these two kinds of interactions to understand the nonmonotonic trend of $\Delta\Theta_{fr}$ shown in Fig. 7(b).

For two charged particles in contact, the magnitude of the contact force can be estimated by the critical pull-off force $F_C = 3\pi\gamma R$ given in Eq. (A2) because the tensile force must exceed F_C before two contacting particles detach. The critical values of other contact force and torques are also related to F_C [50]. Additionally, the Coulomb force can be used to estimate the magnitude of the electrostatic interaction, even though it does not consider the contribution of induced charge [51]. The electrostatic force can thus be estimated as

$$F_E = \frac{q^2}{4\pi\varepsilon_0(2r_p)^2} = \frac{\pi r_p^2 \sigma_0^2}{\varepsilon_0}. \qquad (27)$$

Taking in the physically relevant parameters from Table I then yields

$$\frac{F_E}{F_C} \ll 1, \qquad (28)$$

indicating that the contact force governs when particles are in contact.

To verify Eq. (28), the exponential charge distribution in Fig. 4 is assigned to the initial agglomerate at rest. By simulating the agglomerate restructuring, we focus on the effects of the electrostatic interaction on the interparticle contact force distribution.

Driven by the electrostatic interaction, the agglomerate starts to adjust its structure when the simulation starts. However, only minor adjustments are observed. After reaching a new equilibrium state, the structure no longer changes. Consequently, the final structure formed by charged particles [Fig. 8(c)] is very similar to the original neutral one [Fig. 8(a)]. We then examine the distribution of the normal contact force within the agglomerate. The normal contact force between
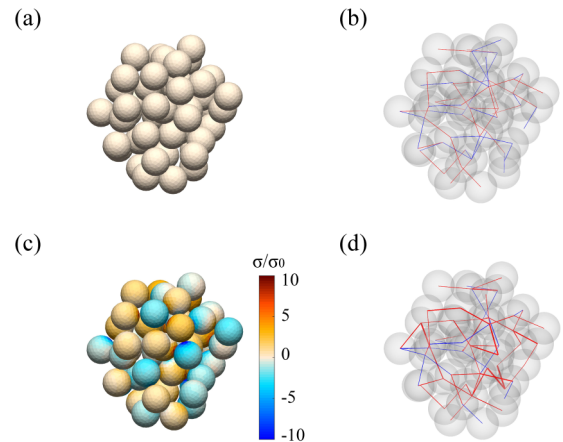

FIG. 8. Left panel: The equilibrium structure formed by (a) neutral and (c) charged particles ($\kappa_p = 10$). Right panel: Force chains of the normal contact force within the agglomerate for (b) neutral and (d) charged particles ($\kappa_p = 10$).
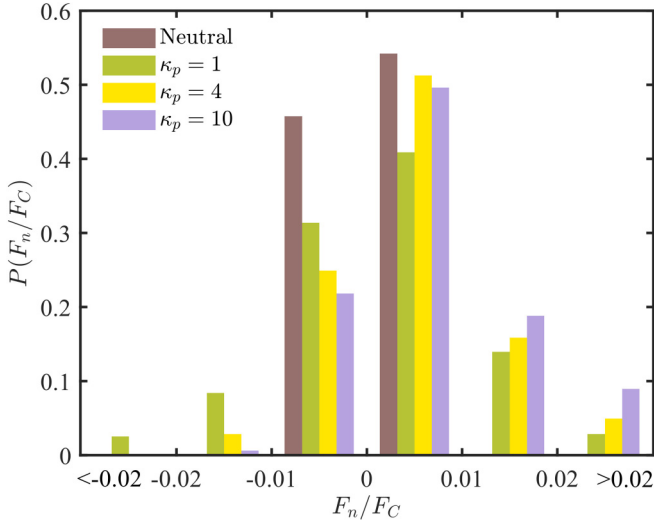
FIG. 9. Probability distribution of the normal contact force.

each contacting particle pair is extracted and plotted as the force-carrying network in Figs. 8(b) and 8(d). Here, the compressive forces are colored in red, while the tensile forces are colored in blue. The line width of each chain is proportional to the force magnitude. For neutral particles, the ratio of compressive and tensile forces is similar, and the force magnitude is relatively small. In comparison, charged particles have a stronger tendency to attract or repel each other, so larger contact forces are required to balance the electrostatic force. Furthermore, most of the normal forces are compressive when $\kappa_p = 10$ [Fig. 8(d)], suggesting that particles tend to compress each other under this condition.

To study the effect of different polarization levels, various particle dielectric constants ($\kappa_p = 1/4/10$) are employed to simulate the restructuring of agglomerate at rest. For each κ_p, parallel simulations are run using 10 realizations of the exponential charge distribution to ensure meaningful statistics. Figure 9 compares the probability distribution function (PDF) of the normal contact force F_n normalized by F_C for neutral and charged particles. For neutral particles, the internal stress can be effectively released, so the force magnitude is small ($|F_n|/F_C < 0.01$). Also, the compressive forces ($F_n > 0$) and the tensile forces ($F_n < 0$) take comparable proportions. For charged particles, since opposite-sign particles could attract each other, the normal overlap δ_n gets larger, giving rise to stronger elastic repulsion that balances the electrostatic attraction. For same-sign particles, the opposite trend can be expected, which leads to stronger tensile force. As a result, the magnitude of the contact force becomes larger, resulting in wider PDFs of F_n/F_C for charged particles.

When comparing results of different κ_p, the PDF of $\kappa_p = 1$ is roughly symmetric about the zero point. Since particles cannot be polarized when $\kappa_p = 1$, the electrostatic force reduces to the pairwise Coulomb force, whose magnitude only depends on the charge amount as $F_{\mathrm{Coul}} \propto |q_1 q_2|/4\pi\varepsilon_0 r^2$. Therefore, the symmetric charge distribution in Fig. 4 will introduce an equal magnitude of electrostatic repulsion and attraction between particles, which eventually leads to the symmetric PDF of F_n. When $\kappa_p > 1$, particle polarization will

modify the electrostatic repulsion and attraction in different ways. For identically charged particles, the surface charge will be pushed to the far side as two particles are pretty close (top insets in Fig. 15). Hence, the effective separation distance between the net charge q_1 and q_2 increases, weakening the electrostatic repulsion. In contrast, the surface charge will shift to the near side between oppositely charged particles (bottom insets in Fig. 15), which significantly reduces the effective separation distance between the net charge and enhances the electrostatic attraction. Thus, as κ_p becomes larger, the PDFs shift toward the direction of positive F_n, revealing stronger interparticle compression.

Even though the contact force between charged particles is stronger than the neutral case, the magnitude of F_n/F_C is still of the order of $O(10^{-2})$. Since the tensile force must satisfy $F_n/F_C \leqslant -1$ before the contact could break, the electrostatic force is still too weak to cause significant restructuring or fragmentation, which validates the estimation of Eq. (28).

In addition to the force ratio F_E/F_C, it is desired to also compare the energy ratio E_E/E_C because particles must overcome the energy barriers associated with contact and electrostatic interactions if they want to move away from each other. The energy barrier caused by the van der Waals adhesion, or the first-contact loss, can be evaluated by multiplying the critical pull-off force F_C and the pull-off distance δ_C in Eq. (A2) [65,66]:

$$E_C \sim F_C \delta_C = 24 \left(\frac{\gamma^5 R^4}{E^2} \right)^{1/3}, \qquad (29)$$

while the energy required to separate two oppositely charged particles can be obtained by integrating the Coulomb force over the long interaction range:

$$E_E \sim \int_{d_p}^{\infty} F_E \, dr = \frac{\pi r_p^3 \sigma_0^2}{2\varepsilon_0}. \qquad (30)$$

Substituting the parameter in Table I gives

$$\frac{E_E}{E_C} \gg 1. \qquad (31)$$

Comparing Eqs. (28) and (31) shows that, even though the electrostatic force is much smaller than the contact force, the energy change caused by the electrostatic force is predominant. This feature can be attributed to the significant difference in the interaction ranges of these two interactions. The short-range contact interaction only affects particle behavior if particles are in contact. When two particles are separating, the longest interaction distance is the pull-off distance δ_C, which is still much smaller than the particle size r_p. Thus, when integrating the normal contact force F_n over its interaction range δ_C, the energy barrier E_C is still limited. In contrast, the long-range electrostatic force decays much slower and remains nonnegligible within a long separation distance. Hence, the electrical energy barrier is orders of magnitude higher than the short-range adhesion.

In addition to the first-contact loss caused by the short-range adhesion E_C and the electrical energy barrier E_E, a certain amount of incident kinetic energy is dissipated by the dissipation forces/torques and the frictions between contact-
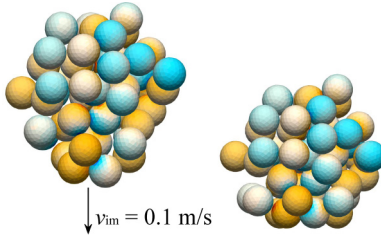
FIG. 10. Agglomerate structures before and after the collision at $v_{\rm im} = 0.1$ m/s and $\kappa_p = 10$. The color bar is the same as Fig. 5.

ing particles, which cannot be estimated directly from scaling analysis because it depends on the force-displacement history of each collision. However, since the initial agglomerate structure and the impact points on the surface are set identical, the energy dissipated by the damping forces/torques and frictions in neutral and charged cases will not vary significantly. Therefore, the distinct collision outcomes shown in Fig. 7(a) are caused by the introduction of the electrostatic interaction.

C. Dominant factors under different incident velocity

Based on the analysis above, we discuss the governing factors under different $v_{\rm im}$. When the incident velocity is low ($v_{\rm im} \leqslant 0.1$ m/s), only the contacts near the impact point are broken, and new ones are formed soon. As a result, the initial agglomerate is only locally compressed near the impact point (Fig. 10). To better illustrate the agglomerate restructuring in the collision, we define the number of contacts between same-sign particles as $N_{\rm C}^{\rm id}$, so the relative change of $N_{\rm C}^{\rm id}$ is

$$f_{\rm C,id} = \frac{N_{\rm C}^{\rm id} - N_{\rm C,0}^{\rm id}}{N_{\rm C,0}^{\rm id}}, \qquad (32)$$

where the subscript 0 refers to the initial value before the collision. The number of contacts between opposite-sign particles and its relative change can be defined similarly as $N_{\rm C}^{\rm op}$ and $f_{\rm C,op}$.

Figure 11(a) plots the relative change of the number of contacts between both same-sign and opposite-sign particles as a function of $v_{\rm im}$. In the low-$v_{\rm im}$ range ($v_{\rm im} \leqslant 0.1$ m/s), both $f_{\rm C,id}$ and $f_{\rm C,op}$ are observed to rise after the compression. Because of the electrostatic attraction between opposite-sign particles, the increase of $f_{\rm C,op}$ is more significant, which also reduces the electric energy of the system ($\Delta U < 0$) in Fig. 11(b). Since new contacts are formed soon after the initial contact breakup, the charged particles are bound tightly by the contact interaction. Thus, the electrostatic interaction cannot drastically alter the collision outcomes within the low-$v_{\rm im}$ regime.

If the incident velocity becomes larger and lies within the moderate range ($v_{\rm im} \sim 0.2$ m/s), the incident kinetic energy is sufficient to break most of the contacts in the original agglomerates. As a result, most particles exist in the form of singlets shortly after the collision, as indicated by the instant at $t = 0.02$ s in Fig. 6. Nevertheless, the kinetic energy is not high enough for particles to overcome the electrical energy barrier and escape. Instead, these particles stay close to each other and start to self-organize. Driven by the electrostatic force, opposite-sign particles tend to attract each other, while same-
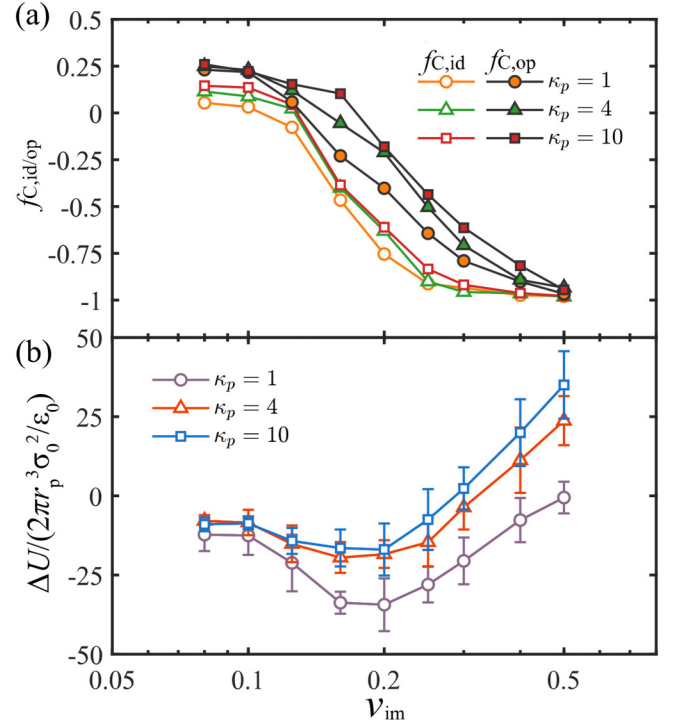

FIG. 11. (a) Relative change of the contact number between same/opposite-sign particles $f_{\rm C,id/op}$ and (b) change of the normalized electrostatic potential energy $\Delta U/(2\pi r_p^3 \sigma_0^2/\varepsilon_0)$ at different $v_{\rm im}$. Error bars in (a) are not shown for clarity.

sign particles are likely to repel each other, both of which minimize the electrical energy of the system [Fig. 11(b)]. When the self-organization is finished, $N_{\rm C}^{\rm id}$ reduces more drastically compared with $N_{\rm C}^{\rm op}$ [Fig. 11(a)], leading to a staggered arrangement of positive and negative particles in the agglomerate. Furthermore, for the same $v_{\rm im}$, both $f_{\rm C,id}$ and $f_{\rm C,op}$ exhibit slighter increase as κ_p rises [Fig. 11(a)]. This can be explained by the enhancement of the pairwise electrostatic attraction and the weakening of the repulsion due to particle polarization (insets of Fig. 15). Therefore, the contacts between both same-sign and opposite-sign particles are more likely to retain after the collision.

It is worth noting that the electrostatic problem becomes highly coupled when considering particle polarization because a charged particle could polarize surrounding particles, and in return, it also becomes polarized. Consequently, the complicated electrostatic interaction between multiple particles cannot be predicted by the simple Coulomb interaction. Figure 12 displays the schematic of typical postcollision fragments containing particles with large charging densities. The numbers in Fig. 12 refer to the free charge density σ_f with units of μC/m^2, and the color denotes the normalized surface charge density σ/σ_0 given in Fig. 5. In Fig. 12(a), the target particle denoted by the red arrow carries a positive net charge ($\sigma_f = 5\,\mu$C/m^2). Since the nearby particles are highly charged, the target particle is significantly polarized, and a clear separation of the negative and positive charge can be observed. As a result, the surface charge is negative in the region near the positive neighbor, leading to the electrostatic attraction between two same-sign particles. Similarly,
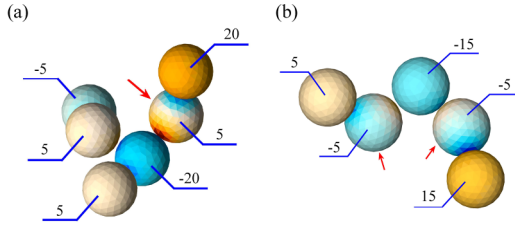
FIG. 12. Fragments containing highly charged particles. The color bar is the same as Fig. 5.

FIG. 13. Schematic of the impact breakage of charged agglomerates. Green bars denote interparticle contacts.

the electrostatic force also becomes attractive between two target particles (denoted by the red arrows) and their same-sign neighbors in Fig. 12(b). This observation highlights the influence of highly charged particles in agglomeration because such particles could polarize neighboring particles and promote particle sticking [44,45].

Finally, if the incident velocity is high ($v_{im} \sim 0.5$ m/s), each particle could obtain sufficient kinetic energy to escape, giving rise to the complete fragmentation of the initial agglomerate. Here, $f_{C,id}$ and $f_{C,op}$ thus approach -1 as v_{im} is large enough [Fig. 11(a)]. As for the change of the electrical energy [Fig. 11(b)], ΔU rises as κ_p increases, indicating a rapid growth of the electrical energy barrier for polarizable particles. Nevertheless, since the kinetic energy prevails, particles will eventually separate, and the fragmentation ratio Θ_{fr} in Fig. 7(a) is close to unity for $v_{im} \sim 0.5$ m/s.

IV. CONCLUSIONS

By employing the BEM-DEM coupled simulation, the impact breakage of the agglomerate formed by tribocharged particles is investigated. Compared with neutral conditions, the charged agglomerate undergoes more pronounced re-agglomeration after the impact, which effectively increases the strength of agglomerates. When quantifying the collision outcomes using the fragmentation ratio Θ_{fr}, the change is found to peak at a moderate incident velocity v_{im}. Moreover, if the induced surface charge due to polarization is included, the electrostatic force becomes more attractive, leading to higher resistance against fragmentation. Scaling analysis reveals the dominant role of the short-range contact interaction when particles are in contact, which tightly binds primary particles and retains the original agglomerate structure. The electrostatic interactions are shown to play a major role in the transient breakup and re-agglomeration process, which tend to assemble charged particles into ordered structures. At last, by considering the dominant ranges of both contact and electrostatic interaction, the physical picture of the impact breakage is presented. Initially, the original agglomerate structure is hyperstatic, so each particle is in contact with several neighbors and tightly bound. When the agglomerate is at rest, the contact force is much larger than the electrostatic force, so that the agglomerate can retain its original structure. The interparticle contacts can only be broken by the incident kinetic energy. For a small incident velocity v_{im}, the impact is too weak to cause fragmentation. Instead, the agglomerate is only partially compressed, with all the individual particles bounded by their neighbors through contact interactions
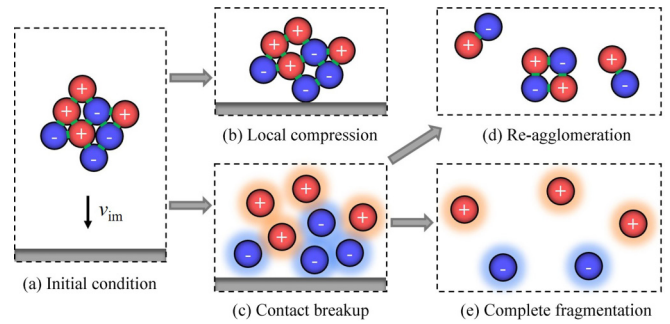
[Fig. 13(b)]. If the collision is energetic enough to destroy the interparticle contacts, particles could move freely under the long-range electrostatic force [Fig. 13(c)]. When the charged particles cannot obtain sufficient velocity to escape, they will be attracted back and rearrange mainly in a positive-negative staggered way [Fig. 13(d)]. On the contrary, single particles with large kinetic energy could escape in a violent collision, causing the complete fragmentation of the initial agglomerates.

In this paper, we focus on the process of wall impact, so the long-range electrostatic interaction only affects particle behavior in the transient breakup and re-organization process. Once new contacts are formed, the fragments will be held together by the short-range contact interactions and do not significantly restructure anymore. If the interparticle contacts can be frequently broken by external forces, such as vibration, charged particles could continuously adjust their position driven by the electrostatic interaction. Eventually, particles carrying opposite charges could mix well, even creating crystalline structures [67,68].

Based on the findings above, several interesting directions can be given. First, this paper focus on the effect of the electrostatic force between charged particles with various levels of polarization. Other conditions, such as the size/shape of the agglomerate or primary particles, the impact angle, and the surface energy density are not considered, so efforts are required to extend this paper to broader parameter spaces and simulation conditions.

Second, the BEM-DEM coupled framework can capture the dynamic evolution of the induced charge when simulating the impact breakage of charged agglomerates containing 50 particles. In terms of computation cost, BEM-DEM supported by FMM-GMRES is more efficient compared with standard BEM-DEM. In future studies, through sophisticated implementation of FMM, the computation cost of BEM can be further reduced (Appendix E), so this framework can be applied to large-scale particulate systems, such as particle packing and agglomeration/aggregation. For the packing and clogging of microparticles [69,70], it has been shown that solely employing the point-charge model [34,36] and the dipole model [37] could already lead to distinct packing structures formed by charged particles. Thus, how the neglected induced higher-order multipoles will affect the final contact network will be worth pursuing. For the agglomeration/aggregation of charged particles [71,72], the electrostatic

force has been reported to significantly extend the bind energy and help overcome the bouncing barrier [41,42], but more efforts are needed to investigate how the induced charge affects the structure and growth rate of agglomerate.

Third, the medium around the particles is assumed to be a vacuum in this paper, so particles are only affected by contact and electrostatic interactions. For applications where particles are immersed in the fluid phase, the particle-fluid interaction must be included [73]. Because of the irregular agglomerate morphology, the associated fluid forces could be complicated [74]. Thus, to extend the current framework to multiphase flow problems with charged solid particles, computational fluid dynamics should be implemented in a sophisticated way to evolve the surrounding flow field and account for the particle-fluid interaction [75,76].

APPENDIX A: NORMAL CONTACT FORCES BETWEEN COLLIDING PARTICLES

As introduced in Sec. II B, the normal contact force contains the normal elastic force F_{ij}^{ne} and the normal dissipation force F_{ij}^{nd}:

$$F_{ij}^{n} = -\left(F_{ij}^{ne} + F_{ij}^{nd}\right) = -4F_C(\hat{a}^3 - \hat{a}^{3/2}) - \eta_n \mathbf{v}_{rel} \cdot \mathbf{n}. \quad (A1)$$

The first term of Eq. (A1) is the normal elastic force. Here, F_C is the critical pull-off force, and $\hat{a} = a/a_0$ is the contact radius a normalized by its value a_0 at the zero-load equilibrium state. Also, $\hat{a}$ can be related to the normal overlap $\delta_N = 2r_{p,c} - |\mathbf{x}_i - \mathbf{x}_j|$ through $\delta_N/\delta_C = 6^{1/3}(2\hat{a}^2 - 4\hat{a}^{1/2}/3)$, where δ_C is the critical pull-off distance, and $r_{p,c}$ is the collision radius. If $\delta_N < -\delta_C$, two contacting particles detach from each other, and the contact interactions are no longer considered. The critical values mentioned above are given as

$$F_C = 3\pi\gamma R, \quad a_0 = \left(\frac{9\pi\gamma R^2}{E}\right)^{1/3}, \quad \delta_C = \frac{a_0^2}{2(6)^{1/3}R}. \quad (A2)$$

Here, γ is the surface energy density, $R = (1/r_i + 1/r_j)^{-1}$ is the effective radius, $E = [(1 - \sigma_{p,i}^2)/E_i + (1 - \sigma_{p,j}^2)/E_j]^{-1}$ is the effective elastic modulus where $\sigma_{p,i}$ and E_i are Poisson's ratio and the elastic modulus of particle i, respectively.

The second term of Eq. (A1) is the normal dissipation force proportional to the normal relative velocity $\mathbf{v}_{rel} \cdot \mathbf{n}$. The normal dissipation coefficient is defined as $\eta_n = \alpha_n(MK_n)^{1/2}$, where α_n is related to the restitution coefficient e, $M = (m_i^{-1} + m_j^{-1})^{-1}$ is the effective mass, and K_n is the normal stiffness coefficient [49,77].
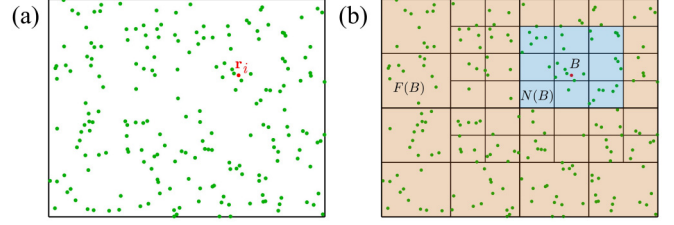

FIG. 14. Schematic of (a) the patch locations and (b) the split of the near-field and the far-field domains.

APPENDIX B: FMM

In this appendix, the general concept of FMM is introduced. In Fig. 14(a), the surface patches (shown as green points) are randomly distributed in the domain. The electric field $\mathbf{E}(\mathbf{r}_i)$ at the location of the target patch $\mathbf{r}_i$ (red point) is

$$\mathbf{E}(\mathbf{r}_i) = \sum_{j \neq i} K(\mathbf{r}_i, \mathbf{r}_j)(\sigma_{f,j} + \sigma_{b,j})a_j, \quad (B1)$$

where $K(\mathbf{r}_i, \mathbf{r}_j) = (\mathbf{r}_i - \mathbf{r}_j)/4\pi\varepsilon_0|\mathbf{r}_i - \mathbf{r}_j|^3$ is the kernel function, $(\sigma_{f,j} + \sigma_{b,j})a_j$ is the net charge on the jth patch.

In FMM, the computation domain is first divided into a tree structure of boxes [Fig. 14(b)]. The original domain is the largest parent box. Then each parent box is further divided into several child boxes until the lowest level is generated. The lowest-level box containing the target patch $\mathbf{r}_i$ is denoted by B. The near field $N(B)$ is defined as the domain occupied by B and its neighboring boxes of the same level [blue-shaded region in Fig. 14(b)], while the rest of the domain is the far field $F(B)$ [brown-shaded region in Fig. 14(b)]. The field strength can thus be split into two parts, the contribution from $N(B)$ and that from $F(B)$:

$$\mathbf{E}(\mathbf{r}_i) = \sum_{\mathbf{r}_j \in N(B), j \neq i} K(\mathbf{r}_i, \mathbf{r}_j)(\sigma_{f,j} + \sigma_{b,j})a_j$$
$$+ \sum_{\mathbf{r}_j \in F(B)} K(\mathbf{r}_i, \mathbf{r}_j)(\sigma_{f,j} + \sigma_{b,j})a_j. \quad (B2)$$

Since the patches in $N(B)$ are close to the target location, the first term on the right-hand side of Eq. (B2) is directly computed using Eq. (B1). As for the contribution of $F(B)$, however, it is not necessary to resolve the electric field generated by each far source patch. Instead, the contribution from all the patches within each far box can be approximated using the multipole expansion [56,78,79]. For each target patch, since most of the source patches belong to $F(B)$, the computation cost is significantly reduced. FMM has been applied in previous works to handle the many-body electrostatic problems [34,37,80].

APPENDIX C: GMRES

Consider a linear equation:

$$A\mathbf{x} = \mathbf{b}, \quad (C1)$$

where A is a $n \times n$ invertible matrix, and $\mathbf{b}$ is a known vector of size n. It is time consuming to solve the inverse matrix A^{-1} to obtain the solution $\mathbf{x} = A^{-1}\mathbf{b}$. Instead, the idea of GMRES

is to construct a Krylov subspace, in which the approximated solution can be found [81]. This method has been applied in previous studies to solve the electrostatic problem [51,52,55].

In the mth iteration, we first construct the mth-order Krylov subspace $K^{(m)}$ defined by A and $\mathbf{b}$:

$$K^{(m)} = \text{span}\{\mathbf{b}, A\mathbf{b}, ..., A^{m-1}\mathbf{b}\}, \quad (C2)$$

where $\mathbf{b}$, $A\mathbf{b}$, …, $A^{m-1}\mathbf{b}$ are the basis vectors of $K^{(m)}$. Then the approximated solution in $K^{(m)}$, which is written as

$$\mathbf{x}^{(m)} = \sum_{i=1}^{m} \alpha_i^{(m)} A^{i-1}\mathbf{b}, \quad (C3)$$

with $\alpha_i^{(m)}$ being the coordinate of the ith basis vector $A^{i-1}\mathbf{b}$, is determined using the least square method to minimize the norm of the residual:

$$|\mathbf{r}^{(m)}| = |\mathbf{b} - A\mathbf{x}^{(m)}|. \quad (C4)$$

If $|\mathbf{r}^{(m)}|$ is smaller than the preset criterion, the approximated solution $\mathbf{x}^{(m)}$ is sufficiently close to the exact solution $\mathbf{x}$, so $\mathbf{x}^{(m)}$ is output as the final solution.

If $|\mathbf{r}^{(m)}|$ is still large, the $(m+1)$th iteration is initiated. The $(m+1)$th basis vector $A^m\mathbf{b}$ is first computed through the matrix-vector product:

$$A \times A^{m-1}\mathbf{b} = A^m\mathbf{b}. \quad (C5)$$

Here, the mth basis vector $A^{m-1}\mathbf{b}$ is already known in the mth iteration. Then the $(m+1)$th-order Krylov subspace $K^{(m+1)}$ is constructed to find the new approximated solution $\mathbf{x}^{(m+1)}$. Because $K^{(m)}$ is a subspace of $K^{(m+1)}$, the norm of the residual will continue to decrease after each iteration as $|\mathbf{r}^{(m+1)}| \leqslant |\mathbf{r}^{(m)}|$.

Since the basis vectors $\mathbf{b}$, $A\mathbf{b}$, …, $A^{m-1}\mathbf{b}$ could capture the dominant eigenvectors of the matrix A, the dimension of $K^{(m)}$ is much smaller than the dimension of the system when the iteration converges, i.e., $m \ll n$, which means the number of iterations required is generally small. In addition, the most expensive calculation in GMRES is the matrix-vector product [Eq. (C5)], which is of the order of O(n^2) for a dense matrix A.

APPENDIX D: INTERACTION ENERGY BETWEEN CHARGED DIELECTRIC PARTICLES

The total electrostatic potential energy of the system can be computed by

$$U = \frac{1}{2} \int_S \sigma_f(\mathbf{r}) \psi(\mathbf{r}) dS. \quad (D1)$$

Here, $\psi(\mathbf{r})$ is the electric potential at position $\mathbf{r}$, and S refers to all surfaces in the system. However, not all the potential energy can be converted to or from the kinetic energy of the particles. We take the example of two identically/oppositely charged particles. The free charge density is set as $\sigma_f = \sigma_0$ for the positive particle and $\sigma_f = -\sigma_0$ for the negative particle. The dielectric constant of particle is $\kappa_p = 10$. Figure 15 displays the normalized potential energy U/U_0 as a function of d/r_p, with d being the surface-to-surface distance between two particles and $U_0 = 2\pi r_p^3 \sigma_0^2 / \varepsilon_0$ being the characteristic potential energy. As the surface-to-surface
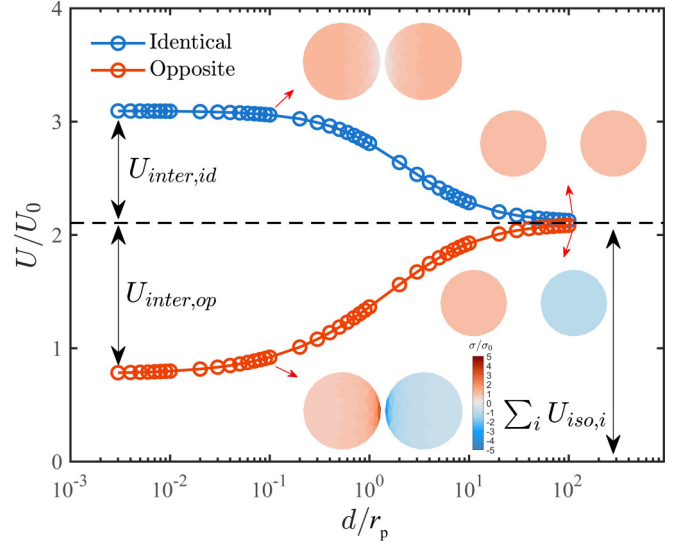

FIG. 15. Dependence of the normalized electrostatic energy U/U_0 on the distance d/r_p between two identically/oppositely charged particles for $\kappa_p = 10$. Insets display the distribution of the normalized surface charge density σ/σ_0.

distance d increases, the normalized energy U/U_0 approaches a constant but nonzero value. At this large separation distance, the electrostatic interaction between these two particles is negligible, so each particle can be treated as an isolated particle with an isolated potential energy:

$$U_{\text{iso},i} = \frac{1}{2} \int_{S_i} \sigma_f(\mathbf{r}) \psi_{\text{iso}}(\mathbf{r}) dS_i. \quad (D2)$$

Here, $\psi_{\text{iso}}(\mathbf{r})$ is the electric potential at position $\mathbf{r}$ generated solely by the surface charge of the isolated particle i. Therefore, $U_{\text{iso},i}$ only shifts the total potential energy by a specific value but does not affect particle behavior. As a result, the interaction energy U_{inter} can be obtained by subtracting the isolated energy of all the individual particles from the total potential energy U:

$$U_{\text{inter}} = U - \sum_{i=1}^{N_p} U_{\text{iso},i}. \quad (D3)$$

Here, U_{inter} measures the electrostatic energy that is consequential to the interaction between charged particles and is thus employed in the discussion.

APPENDIX E: COMPARISON OF WALL TIME

Table II lists the wall time of different cases shown in Fig. 5. The simulated duration is $T = 0.085$ s in physical

TABLE II. Wall time of typical simulations.

Cases	Wall time t_{wall} (s)	
	Mean value	Standard deviation
Neutral	2674.2	356.8
$\kappa_p = 1$	8018.1	732.7
$\kappa_p = 4$	28 059.9	1062.8
$\kappa_p = 10$	36 946.4	1508.6

space, which is equal to 8500 electrical time steps dt_E or 340 000 collision time steps dt_C in the simulation. For the same case, the wall times are averaged among parallel runs and presented in the form of the mean value and the standard deviation.

In the neutral cases, the BEM calculation is ignored, so we only need to resolve the contact interactions between each pair of colliding particles. The computation cost is therefore related to the total number of particles N_p. In comparison, for charged particles, we must consider the interaction between each pair of surface patches, so the cost of the BEM is determined by the total number of surface patches in the system $N_{tot} = N_p \times N_{pat}$, with N_{pat} being the patch number on each particle. Since N_{pat} is generally of the order of $O(10^2)$–$O(10^3)$, the cost of the BEM is most expensive in this paper. In the previous work [51], the calculation cost of the BEM in two simple cases have been discussed. When only using GMRES in the BEM, the cost scales as $O(N_{tot}^2)$. If the GMRES-FMM

coupled method is applied, the cost is found to reduce to $O(N_{tot}^{1.333})$ and $O(N_{tot}^{1.564})$. In future investigations, the cost can be further reduced by optimizing the tree structure generated in FMM [80], applying the parallel FMM [79], or using the plane-wave-based operators [78,82]. The calculation could be expected to scale as $O(N_{tot})$, so this framework could be applied to large-scale particulate systems.

In addition, one can observe that the wall time increases with the particle dielectric constant κ_p. If $\kappa_p = 1$, since $\kappa_p = \kappa_0$, the right-hand-side vector in Eq. (10) is **b** = 0. In this case, Eq. (10) directly leads to the zero induced charge. We only need to call FMM once to calculate the field strength generated by the free charge [Eq. (5) or Eq. (18)]. The electrostatic force/torque can then be obtained using Eq. (11). However, if $\kappa_p > 1$, the vector **b** in Eq. (10) becomes nonzero, so a GMRES-FMM iteration must be conducted to solve the induced charge σ_b. With the increase of κ_p, more iterations are needed before σ_b converges, which requires more computation time.

[1] J. Israelachvili, *Intermolecular and Surface Forces* (Academic Press, Cambridge, 2011).

[2] S. Chen, S. Li, and J. Marshall, Exponential scaling in early-stage agglomeration of adhesive particles in turbulence, Phys. Rev. Fluids **4**, 024304 (2019).

[3] Z. Fang, Y. Zhang, X. Wu, L. Sun, and S. Li, New explicit correlations for the critical sticking velocity and restitution coefficient of small adhesive particles: a finite element study and validation, J. Aero. Sci. **160**, 105918 (2022).

[4] J. Blum and G. Wurm, The growth mechanisms of macroscopic bodies in protoplanetary disks, Annu. Rev. Astron. Astrophys. **46**, 21 (2008).

[5] G. Wurm and J. Teiser, Understanding planet formation using microgravity experiments, Nat. Rev. Phys. **3**, 405 (2021).

[6] A. Jaworek, A. Marcchewicz, A. Sobczyk, A. Krupa, and T. Czech, Two-stage electrostatic precipitators for the reduction of PM2.5 particle emission, Prog. Energy Combust. Sci. **67**, 206 (2018).

[7] Z. Sun Z, L. Yang, A. Shen, L. Zhou L, and H. Wu, Combined effect of chemical and turbulent agglomeration on improving the removal of fine particles by different coupling mode, Powder Technol. **344**, 242 (2019).

[8] P. Begat, D. Morton, J. Staniforth, and R. Price, The cohesive-adhesive balances in dry powder inhaler formulations II: influence on fine particle delivery characteristic, Pharm. Res. **21**, 1826 (2004).

[9] J. Yang, C. Wu, and M. Adams, Numerical modelling of agglomeration and deagglomeration in dry powder inhalers: A review, Curr. Pharm. Des. **21**, 5915 (2015).

[10] D. Eskin, J. Ratulowski, K. Akbarzadeh, and S. Pan, Modelling asphaltene deposition in turbulent pipeline flows, Can. J. Chem. Eng. **89**, 421 (2011).

[11] W. Liu and C. Wu, Migration and agglomeration of adhesive microparticle suspensions in a pressure-driven duct flow, AIChE J. **66**, e16974 (2020).

[12] K. Higashitani, K. Iimura, and H. Sanda, Simulation of deformation and breakup of large aggregates in flows of viscous fluids, Chem. Eng. Sci. **56**, 2927 (2001).

[13] C. Marshioli and A. Soldati, Turbulent breakage of ductile aggregates, Phys. Rev. E **91**, 053003 (2015).

[14] X. Ruan, S. Chen, and S. Li, Structural evolution and breakage of dense agglomerates in shear flow and Taylor-Green vortex, Chem. Eng. Sci. **211**, 115261 (2020).

[15] G. Frungieri and M. Vanni, Aggregation and breakup of colloidal particle aggregates in shear flow: A combined Monte Carlo-Stokesian dynamics approach, Powder Technol. **388**, 357 (2021).

[16] Y. Yao and J. Capecelatro, Deagglomeration of cohesive particles by turbulence, J. Fluid Mech. **911**, A10 (2021).

[17] K. Zhao, F. Pomes, B. Vowinckel, T. Hsu, B. Bai, and E. Meiburg, Flocculation of suspended cohesive particles in homogeneous isotropic turbulence, J. Fluid Mech. **921**, A17 (2021).

[18] P. Liu and C. Hrenya, Cluster-Induced Deagglomeration in Dilute Gravity-Driven Gas-Solid Flows of Cohesive Grains, Phys. Rev. Lett. **121**, 238001 (2018).

[19] S. Chen and S. Li, Collision-induced breakage of agglomerates in homogenous isotropic turbulence laden with adhesive particles, J. Fluid Mech. **902**, A28 (2020).

[20] A. Khalifa and M. Breuer, Data-driven model for the breakage of dry monodisperse agglomerates by wall impact applicable for multiphase flow simulations, Powder Technol. **376**, 241 (2020).

[21] H. Chen, W. Liu, Z. Zheng, and S. Li, Impact dynamics of wet agglomerates onto rigid surfaces, Powder Technol. **379**, 296 (2021).

[22] A. Khalifa and M. Breuer, An efficient model for the breakage of agglomerates by wall impact applied to Euler-Lagrange LES predictions, Int. J. Multiph. Flow **142**, 103625 (2021).

[23] C. Thornton, K. Yin, and M. Adams, Numerical simulation of the impact fracture and fragmentation of agglomerates, J. Phys. D: Appl. Phys. **29**, 424 (1996).

[24] R. Moreno-Atanasio and M. Ghadiri, Mechanistic analysis and computer simulation of impact breakage of agglomerates: Effect of surface energy, Chem. Eng. Sci. **61**, 2476 (2006).

[25] A. Voss and W. Finlay, Deagglomeration of dry powder pharmaceutical aerosols, Int. J. Pham. **248**, 39 (2002).

[26] K. Iimura, M. Suzuki, M. Hirota, and K. Higashitani, Simulation of dispersion of agglomerates in gas phase–acceleration field and impact on cylindrical obstacle, Adv. Powder Technol. **20**, 210 (2009).

[27] Z. Tong, R. Yang, and A. Yu, Numerical modelling of the breakage of loose agglomerates of fine particles, Powder Technol. **196**, 213 (2009).

[28] L. Liu, K. Kafui, and C. Thornton, Impact breakage of spherical, cuboidal and cylindrical agglomerates, Powder Technol. **199**, 189 (2010).

[29] X. Deng and R. Davé, Breakage of fractal agglomerates, Chem. Eng. Sci. **161**, 117 (2017).

[30] J. Yang, L. Bello, K. Buettner, Y. Guo, C. Wassgren, and J. Curtis, Breakage of wet flexible fiber agglomerates impacting a plane, AIChE J. **65**, 16626 (2019).

[31] K. Forward, D. Lacks, and R. Sankaran, Charge Segregation Depends on Particle Size in Triboelectrically Charged Granular Materials, Phys. Rev. Lett. **102**, 028001 (2009).

[32] S. Waitukaitis, V. Lee, J. Pierson, S. Forman, and H. Jaeger, Size-Dependent Same-Material Tribocharging in Insulating Grains, Phys. Rev. Lett. **112**, 218001 (2014).

[33] J. Haeberle, A. Schella, M. Sperl, M. Schöter, and P. Born, Double origin of stochastic granular tribocharging, Soft Matter **14**, 4987 (2018).

[34] S. Chen, S. Li, W. Liu, and H. Makse, Effect of long-range repulsive coulomb interactions on packing structure of adhesive particles, Soft Matter **12**, 1836 (2016).

[35] B. Gryzbowski, A. Winkleman, J. Wiles, Y. Brumer, and G. Whitesides, Electrostatic self-assembly of macroscopic crystals using contact electrification, Nat. Mater. **2**, 241 (2003).

[36] S. Chen, W. Liu, and S. Li, Effect of long-range electrostatic repulsion on pore clogging during microfiltration, Phys. Rev. E **94**, 063108 (2016).

[37] X. Qian, X. Ruan, and S. Li, Effect of interparticle dipolar interaction on pore clogging during microfiltration, Phys. Rev. E **105**, 015102 (2022).

[38] X. Ruan, S. Chen, and S. Li, Effect of long-range coulomb repulsion on adhesive particle agglomeration in homogeneous isotropic turbulence, J. Fluid Mech. **915**, A131 (2021).

[39] F. Jalalinejad, X. Bi, and J. Grace, Effect of electrostatics on freely-bubbling beds of mono-sized particles, Int. J. Multiph. Flow **70**, 104 (2015).

[40] C. Pei, C. Wu, and M. Adams, DEM-CFD analysis of contact electrification and electrostatic interactions during fluidization, Powder Technol. **304**, 208 (2016).

[41] V. Lee, S. Waitukaitis, M. Miskin, and H. Jaeger, Direct observation of particle interactions and clustering in charged granular streams, Nature Phys. **11**, 733 (2015).

[42] T. Steinpiltz, K. Joeris, F. Jungmann, D. Wolf, L. Brendel, J. Teiser, T. Shinbrot, and G. Wurm, Electrical charging overcomes the bouncing barrier in planet formation, Nature Phys. **16**, 225 (2020).

[43] J. Kolehmainen, A. Ozel, Y. Gu, T. Shinbrot, and S. Sundaresan, Effects of Polarization on Particle-Laden Flows, Phys. Rev. Lett. **121**, 124503 (2018).

[44] J. Feng, Electrostatic interaction between two charged dielectric spheres in contact, Phys. Rev. E **62**, 2891 (2000).

[45] A. Matias, T. Shinbrot, and N. Araújo, Mechanical equilibrium of aggregates of dielectric spheres, Phys. Rev. E **98**, 062903 (2018).

[46] S. Li and J. Marshall, Discrete element simulation of microparticle deposition on a cylindrical fiber in an array, J. Aerosol Sci. **38**, 1031 (2007).

[47] S. Li, J. Marshall, G. Liu, and Q. Yao, Adhesive particulate flow: the discrete-element method and its application in energy and environmental engineering, Prog. Energy Combust. Sci. **37**, 633 (2011).

[48] K. Johnson, K. Kendall, and A. Roberts, Surface energy and the contact of elastic solids, Proc. R. Soc. London A **324**, 301 (1971).

[49] Y. Tsuji, T. Tanaka, and T. Ishida, Lagrangian numerical simulation of plug flow of cohesionless particles in a horizontal pipe, Powder Technol. **71**, 239 (1992).

[50] J. Marshall and S. Li, *Adhesive Particle Flows: A Discrete-Element Approach* (Cambridge University Press, Cambridge, 2014).

[51] X. Ruan, M. Gorman, S. Li, and R. Ni, Surface-resolved dynamic simulation of charged non-spherical particles, J. Compt. Phys. **466**, 111381 (2022).

[52] K. Barros, D. Sinkovits, and E. Luijten, Efficient and accurate simulation of dynamic dielectric objects, J. Chem. Phys. **140**, 064903 (2014).

[53] D. Lacks and T. Shinbrot, Long-standing and unresolved issues in triboelectric charging, Nat. Rev. Chem. **3**, 465 (2019).

[54] P. Persson and G. Strang, A simple mesh generator in MATLAB, SIAM Rev. **46**, 329 (2004).

[55] K. Barros and E. Luijten, Dielectric Effects in the Self-Assembly of Binary Colloidal Aggregates, Phys. Rev. Lett. **113**, 017801 (2014).

[56] L. Greengard and V. Rokhlin, A fast algorithm for particle simulations, J. Compt. Phys. **73**, 325 (1987).

[57] See, https://github.com/zgimbutas/fmmlib3d.

[58] Z. Gimbutas and L. Greengard, Simple FMM libraries for electrostatics, slow viscous flow, and frequency-domain wave propagation, Commun. Comput. Phys. **18**, 516 (2015).

[59] L. Liu, Z. Zhang, and A. Yu, Dynamic simulation of the centripetal packing of mono-sized spheres, Physica A **268**, 433 (1999).

[60] G. Liu, J. Marshall, S. Li, and Q. Yao, Discrete-element method for particle capture by a body in an electrostatic field, Int. J. Numer. Meth. Engng. **84**, 1589 (2010).

[61] Y. Yao and J. Capecelatro, An accurate particle-mesh method for simulating charged particles in wall-bounded flows, Powder Technol. **387**, 239 (2021).

[62] U. Konopka, F. Mokler, A. Ivlev, M. Kretschmer, G. Morfill, H. Thomas, H. Rothermel, V. Fortov, A. Lipaev, V. Molotkov *et al.*, Charge-induced gelation of microparticles, New J. Phys. **7**, 227 (2005).

[63] S. Soh, S. Kwok, H. Liu, and G. Whitesides, Contact de-electrification of electrostatically charged polymers, J. Am. Chem. Soc. **134**, 20151 (2012).

[64] C. Thornton and K. Yin, Impact of elastic spheres with and without adhesion, Powder Technol. **65**, 153 (1991).

[65] G. Liu, S. Li, and Q. Yao, A JKR-based dynamic model for the impact of micro-particle with a flat surface, Powder Technol. **207**, 215 (2011).

[66] S. Chen, S. Li, and M. Yang, Sticking/rebound criterion for collisions of small adhesive particles: Effects of impact parameter and particle size, Powder Technol. **274**, 431 (2015).

[67] A. Schella, S. Weis, and M. Schröter, Charging changes contact composition in binary sphere packing, Phys. Rev. E **95**, 062903 (2017).

[68] A. Schella, S. Herminhaus, and M. Schröter, Influence of humidity on tribo-electric charging and segregation in shaken granular media, Soft Matter **13**, 394 (2017).

[69] W. Liu, Y. Jin Y, S. Chen, H. Makse, and S. Li, Equation of state for random sphere packings with arbitrary adhesion and friction, Soft Matter **13**, 421 (2017).

[70] D. Wang, J. Treado, A. Boromand, B. Norwick, M. Murrell, M. Shattuck, and C. O'Hern, The structural, vibrational, and mechanical properties of jammed packings of deformable particles in three dimensions, Soft Matter **17**, 9901 (2021).

[71] F. Jungmann and G. Wurm, Observation of bottom-up formation for charged grain aggregates related to pre-planetary evolution beyond the bouncing barrier, Astron. Astrophys. **650**, A77 (2021).

[72] F. Jungmann, M. Kruss, J. Teiser, and G. Wurm, Aggregation of sub-mm particles in strong electric fields under microgravity conditions, Icarus **373**, 114766 (2022).

[73] Z. Fang, Y. Zhang, S. Zhao, X. Li, X. Wu, and L. Sun, An experimental investigation on the settling velocity and drag coefficient of micrometer-sized natural, IG-110, NG-CT-10 and A3-3 graphite particles, J. Aero. Sci. **155**, 105774 (2021).

[74] S. Chen, P. Chen, and J. Fu, Drag and lift forces acting on linear and irregular agglomerates formed by spherical particles, Phys. Fluids. **34**, 023307 (2022).

[75] W. Liu and C. Wu, Analysis of inertial migration of neutrally buoyant particle suspensions in a planar Poiseuille flow with a coupled lattice Boltzmann method-discrete element method, Phys. Fluids **31**, 063301 (2019).

[76] Y. Shao Y, X. Ruan, and S. Li, Mechanism for clogging of microchannels by small particles with liquid cohesion, AIChE J. **67**, e17288 (2021).

[77] J. Marshall, Discrete-element modeling of particulate aerosol flows, J. Compt. Phys. **228**, 1541 (2009).

[78] L. Greengard and V. Rokhlin, A new version of the fast multipole method for the Laplace equation in three dimensions, Acta Numer. **6**, 229 (1997).

[79] D. Malhotra and G. Biros, PVFMM: A parallel kernel independent FMM for particle and volume potentials, Commun. Comput. Phys. **18**, 808 (2015).

[80] E. Lindgren, A. Stace, E. Polack, Y. Maday, B. Stamm, and E. Besley, An integral equation approach to calculate electrostatic interaction in many-body dielectric systems, J. Comput. Phys. **371**, 712 (2018).

[81] Y. Saad and M. Schultz, GMRES: A generalized minimum residual algorithm for solving nonsymmetric linear systems, SIAM J. Sci. Stat. Comput. **7**, 856 (1986).

[82] H. Cheng, L. Greengard, and V. Pokhlin, A fast adaptive multipole algorithm in three dimensions, J. Comput. Phys. **155**, 468 (1999).